

Exoplanet Reflected Light Spectroscopy with PICASO

NATASHA E. BATALHA,¹ MARK S. MARLEY,² NIKOLE K. LEWIS,³ AND JONATHAN J. FORTNEY¹

¹*Department of Astronomy and Astrophysics, University of California Santa Cruz, Santa Cruz, CA 95064, USA*

²*NASA Ames Research Center, MS 245-3, Moffett Field, CA 94035, USA*

³*Department of Astronomy and Carl Sagan Institute, Cornell University, 122 Sciences Drive, Ithaca, NY 14853, USA*

(Accepted April 12, 2019)

Submitted to ApJ

ABSTRACT

Here we present the first open-source radiative transfer model for computing the reflected light of exoplanets at any phase geometry, called PICASO: Planetary Intensity Code for Atmospheric Scattering Observations. This code, written in Python, has heritage from a decades old, well-known Fortran model used for several studies of planetary objects within the Solar System and beyond. We have adopted it to include several methodologies for computing both direct and diffuse scattering phase functions, and have added several updates including the ability to compute Raman scattering spectral features. Here we benchmark PICASO against two independent codes and discuss the degree to which the model is sensitive to a user’s specification for various phase functions. Then, we conduct a full information content study of the model across a wide parameter space in temperature, cloud profile, SNR and resolving power.

1. INTRODUCTION

Across all the state-of-the-art pipelines that exist to study atmospheric composition and climate from exoplanets, about half a dozen have been developed for transiting science, a few of which are open-source (e.g. Madhusudhan & Seager 2009; Line et al. 2012; Benneke & Seager 2012; Waldmann et al. 2015; Barstow et al. 2017; Zhang et al. 2019). This abundance of model development has overall improved the quality of all of these models, has contributed to interesting model inter-comparison studies (e.g. Baudino et al. 2017), and increased accessibility of traditionally private codes.

On the other hand, for observations of reflected light from directly imaged exoplanets there have only been two, neither of which are open source (Lupu et al. 2016; Lacy et al. 2019). An additional branch of models, used for Solar System/Earth science also exists to compute reflected light from planetary atmospheres (NEMESIS, Irwin et al. (2008); DISORT, Stamnes et al. (1988); PSG, Villanueva et al. (2018)). NEMESIS is well-vetted, and has been used for retrieving composition from dozens of observations of Jupiter (e.g. Irwin et al. 2019a), Nep-

tune (e.g. Irwin et al. 2019b), Titan (e.g. Thelen et al. 2019) and many more. DISORT is an open-source forward model, however cannot be used to retrieve atmospheric composition. Note that all retrieval models consist of a versatile and fast forward model that can be wrapped in a statistical algorithm. DISORT contains several hard-wired assumptions for terrestrial conditions and is not versatile/fast enough to use in a retrieval framework. PSG is the retrieval tool of the ExoMars mission and has been used for other investigations such as Earth and the NASA Infrared Telescope Facility. Lastly, ray-tracing forward models, such as Dyudina et al. (2016), would also be computationally intensive and complex to wrap into a retrieval framework for exoplanets.

With the detection and analysis of reflected light from optical phase curves (Demory et al. 2013; Esteves et al. 2015; Niraula et al. 2018) and optical photometry (Evans et al. 2013; Barstow et al. 2014; Garcia Munoz & Isaak 2015; Webber et al. 2015; Lee et al. 2017), and the onset of reflected light direct imaging missions on the horizon, such as *WFIRST* and *ELTs*, Spergel et al. (2013), there has been an increasing demand for an accessible, versatile reflected light code.

Here, we present the **Planetary Intensity Code for Atmospheric Scattering Observations** (PICASO). It is

available through `GitHub`¹, and can be installed through `pip` or `conda`. Tutorials for running the code are available online² along with an in-depth physics tutorial for the derivation of the radiative transfer of the code³.

1.1. *The Heritage of the Code*

The methodology of PICASO partly originates from the Fortran albedo spectra model described in several studies of planetary objects within the Solar System (McKay et al. 1989; Marley & McKay 1999) and beyond (Marley et al. 1999). These models utilized radiative transfer methods described in Toon et al. (1977, 1989) and only included the capability to compute monochromatic scattered radiation observed at full phase. Later, Cahoy et al. (2010) introduced the capability to compute the monochromatic scattered radiation observed *at any phase angle*. Since then the model has been widely used in several studies of exoplanets including: retrievals of exoplanet atmospheres (Lupu et al. 2016; Nayak et al. 2017) sulfur hazes in giant exoplanet atmospheres (Gao et al. 2017), Earth analogues in reflected light (Feng et al. 2018), water absorption in cool giants (MacDonald et al. 2018), and color classification of directly imaged exoplanets (Batalha et al. 2018b), among others.

While the code bifurcated across several of these analyses (e.g. updates to molecular opacities, various ways to regrid the atmosphere, varying phase functions, different sources of scattering and cloud opacity) the bulk of the radiative transfer in the code has remained relatively similar since the original publications of McKay et al. (1989); Marley et al. (1999); Cahoy et al. (2010). Individual changes for each analysis lack trace-ability since the age of version control through `GitHub` is a recent phenomenon.

PICASO is the first open-source compilation of all these previous works. It is written in `Python` and is designed to be user-friendly and versatile enough to handle all the use cases that have come before it, and additional use cases yet to be explored.

1.2. *Exoplanet Diversity & the Need for Versatility*

At the foundation of any reflected light code is an assumption of a scattering phase function, $p(\cos \Theta)$, used to describe the angular dependence of how light is scattered. Assumptions of phase functions vary widely in complexity (Hansen 1969). The most simplistic assumption is an isotropic scattering phase function. In this case, there is equal probability of arriving photons trav-

eling to scatter in any given direction. Of course, scattering by gasses and particles is not isotropic. To account for more realistic phase functions, an asymmetry parameter, g , is usually introduced, and used with more complex phase functions. It is important to note that asymmetry values vary widely depending on the specific optical properties of the condensing species (e.g., Morley et al. 2012).

Figure 1 shows distributions of asymmetry parameters and single scattering albedos from a wide range of giant planet models computed in Batalha et al. (2018b) (data is available through Batalha et al. (2018c)). All cloud models were computed using Ackerman & Marley (2001) for a Jupiter-like system ($1 \times$ Solar metallicity, 25 ms^{-2}), with varying semi-major axes (i.e equilibrium temperatures). For reference, the asymmetry parameters of well-studied cirrus clouds and volcanic aerosols are also shown (Thomas & Stamnes 2002).

At 5 AU from a Sun-like star, $\text{H}_2\text{O}/\text{NH}_3$ clouds dominate the optical behavior, leading to high asymmetry values/single scattering albedo. At hotter temperatures more exotic cloud species such as ZnS and Na_2S begin to widen and decrease the distribution of asymmetry values/single scattering albedos. Exoplanet atmospheres, which cover a broad range in mass and temperature space, will exhibit a wide range of optical properties.

To emphasize how these wide ranges of optical properties propagate to the behavior of the phase function, Figure 2 shows a typical phase function computed for a range in asymmetry parameters, g .

The extreme range in these differences motivated the design of the new code. We aimed to create a code where fundamental radiative transfer assumptions, such as that of the phase function, could be easily assessed. We hope that this will guide development of future facilities, and facilitate a symbiotic relationship between future observations and the improvement of theoretical models of directly imaged exoplanets.

1.3. *Organization*

In what follows we describe the methodology of PICASO in §2, with a special emphasis on the new physics/capabilities that have been introduced. Then we will analyze the major assumptions made in our calculations of the reflected light in §3 in order to show which assumptions the calculations are most sensitive to across a large parameter space in planet temperature, cloud composition, and stellar type. In §4 we validate PICASO against two different independent calculations. Then, given the most up-to-date specifics of a future space-based direct imaging mission, we use PICASO to do a full information-content analysis across SNR and

¹ [GitHub](#)

² [Code Tutorial](#)

³ [Physics Tutorial](#)

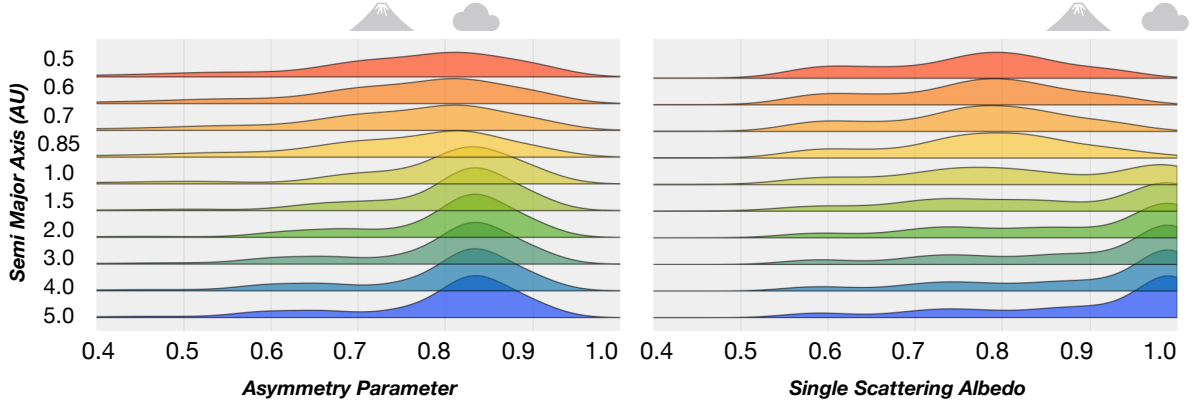


Figure 1. Aggregated asymmetry parameters, and single scattering albedos from the grid of models used in Batalha et al. (2018b). Each distribution showcases the diversity of values we should expect for different temperature exoplanets ranging from semi-major axis= 0.5 – 5 AU. For reference, the cloud icon represents the asymmetry and single scattering of a cirrus cloud, and the volcano icon represents the same of aged volcanic aerosols (Thomas & Stamnes 2002). **Main Point:** Exoplanet atmospheres will exhibit a diverse range in optical properties.

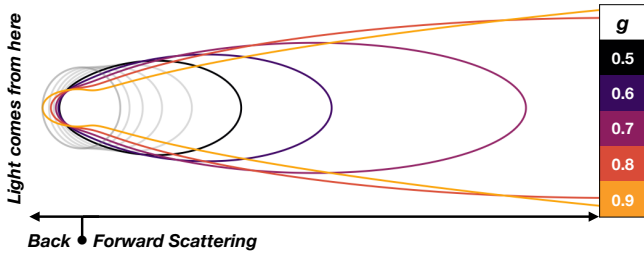


Figure 2. A two-term Henyey-Greenstein phase function for a range of asymmetry values. **Main Point:** Seemingly small changes to g propagate to large differences in the phase function behavior. \mathcal{Q}

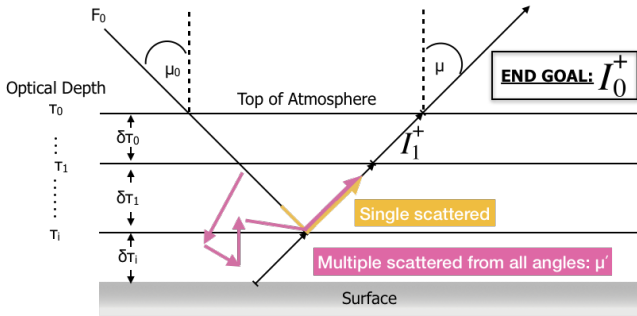


Figure 3. Model schematic of PICASO. \mathcal{Q}

resolving power. Here, we will specifically focus on our ability to constrain atmospheric composition and gravity. We end with a discussion and conclusion in §6.

2. PICASO: THE FORWARD MODEL

A full derivation of the radiative transfer of the forward model can be found [online](#). As is with any atmospheric scattering code, we begin with the radiative transfer equation (Goody & Yung 1989):

$$I(\tau_i, \mu) = I(\tau_{i+1}, \mu) e^{\delta\tau_i/\mu} - \int_0^{\delta\tau_i} S(\tau'\mu) e^{-\tau'/\mu} d\tau'/\mu \quad (1)$$

Here, the terms are as following:

- $I(\tau_i, \mu)$: the azimuthally averaged intensity emergent from the top of an atmospheric layer, i , with opacity, τ , and outgoing angle, μ
- $I(\tau_{i+1}, \mu) e^{\delta\tau_i/\mu}$: the incident intensity on the lower boundary of the layer attenuated by the optical depth *within* the layer, $\delta\tau$
- $S(\tau', \mu)$: the source function, integrated over all layers

In our formalism, the source function only consists of two components: 1) the single-scattered radiation, and 2) the multiple scattered radiation, integrated over all diffuse angles. In other words, we do not include a thermal term in the source function. Traditionally, dating back to (Toon et al. 1989), the thermal and reflected light terms have been computed separately. We leave the addition of the thermal component to a future update so that the source function has the form:

$$S(\tau', \mu) = \frac{\omega}{4\pi} F_0 P_{single}(\mu, -\mu_0) e^{-\tau'/\mu_s} + \frac{\omega}{2} \int_{-1}^1 I(\tau', \mu') P_{multi}(\mu, \mu') d\mu' \quad (2)$$

where the first term is the single-scattered radiation, whose behavior is described by the phase function $P_{single}(\mu, -\mu_0)$, and the second term is the multiple

scattered radiation, whose behavior is described by $P_{multi}(\mu, \mu')$. A schematic of the plane-parallel model is shown in Figure 3.

In addition to basic planetary properties (e.g. stellar spectrum, planet mass & radius) PICASO takes in as input: 1) a pressure-temperature profile and altitude-dependent abundances (see `</>`, `justdoit.atmosphere()`), and 2) a cloud profile (single scattering albedo, asymmetry parameter, and total extinction; see `</>`, `justdoit.clouds()`). As further shown in the tutorial, the cloud profile can either be input as a full altitude dependent profile parameterized or generated from a model such as Ackerman & Marley (2001), or it can be input as different cloud layers that are arbitrarily set by additionally supplying the cloud top pressures and vertical extent of each layer. PICASO is designed to accommodate several different input styles in order to be highly customizable for each user.

Our methodology is thoroughly described in Cahoy et al. (2010) (see Section 3.2). In short, we follow the source function method in Toon et al. (1989). We first use the two-stream quadrature to solve for the diffuse scattered radiation. Then, we use the resulting two-stream intensity to approximate the source function. There are several other methods of solving this, e.g. δ -M stream method (Wiscombe 1977), which we will explore in a future release of the code.

PICASO includes several ways of handling the single and multiple scattering phase functions, as compared with (Cahoy et al. 2010). Additionally, PICASO has been written to include a more physically motivated methodology for Raman Scattering. Therefore, we will devote §2.1, §2.2, & §2.4 to these specific components and we reference Cahoy et al. (2010) for an explanation of the boundary condition formalism, which has not been altered. Finally, in §2.5 & §2.6 we derive the methodology for computing various types of albedos and the planet phase geometry, respectively.

2.1. The Single Scattering Component

For the direct/single scattering component, the most widely used form is the Henyey-Greenstein (HG) phase function because it is: a function of g , generally resembles “real” phase functions, and is non-negative for all values of Θ . The one-term HG phase function has the form:

$$P_{OTHG} = \frac{1 - g^2}{(1 + g^2 - 2g \cos \Theta)^{3/2}} \quad (3)$$

Here, g is the asymmetry parameter, which is defined as:

$$g = \frac{1}{4\pi} \int_{4\pi} p(\cos \Theta) \cos \Theta d\omega \quad (4)$$

where Θ is the angle between the original direction and the scattered direction (related to the planet’s phase, α function via $\alpha = \pi - \Theta$). By defining this parameter, we only need to determine the relative proportion of photons that are scattered in the forward versus backward direction (as opposed to each individual intensity).

The asymmetry parameter, g can be any value $-1 \leq g \leq 1$. In the limit when $g = 1$, photons approximately continue traveling in their original direction, when $g = -1$ their directions are reversed, and when $g = 0$ they are equally likely to travel in the forward or backward direction (i.e. isotropy, \mathbf{Q}).

Using Equation 3 for the single scattering phase function, is easily accessed in PICASO (`</>`), but it is not the default. This is because although Equation 3 captures the observed forward peak relatively well, it fails to capture the additional (albeit smaller) backward scattering peak that has been observed on the Moon, Mars, Venus and Jupiter (Sudarsky et al. 2005). To account for this, a second term in the phase function can be introduced :

$$P_{TTHG}(\cos \Theta) = f P_{OTHG}(\cos \Theta, g_f) + (1 - f) P_{OTHG}(\cos \Theta, g_b). \quad (5)$$

Here, in addition to having two asymmetry factors (g_f for the forward & g_b for the backward), we also have a new parameter, f , which describes the fraction of forward to back scattering. In PICASO, we give f the functional form of

$$f = c_1 + c_2 g_b^{c_3} \quad (6)$$

where users can specify c_1 , c_2 , and c_3 . By default, PICASO, sets $g_f = \bar{g}$, $g_b = -\bar{g}/2$, and $f = 1 - \bar{g}^2$. \bar{g} is the cloud asymmetry factor that is computed directly from the cloud code `eddysed`, weighted by the contribution of cloud opacity ($\bar{g} = g_{cld} \tau_{cld} / \tau_{scat}$) (Ackerman & Marley 2001).

However these values are certainly not universal. Jupiter, Saturn, Uranus and Neptune all exhibit slightly different forward/back scattering peaks (Sudarsky et al. 2005; Dyudina et al. 2016). For observations of exoplanets, these parameters will have to be fit for.

The last component to consider is the effect of Rayleigh scattering, which acts to increase the back scattering peak. The Rayleigh phase function has the form:

$$P_{ray}(\cos \Theta) = \frac{3}{4} (1 + \cos^2 \Theta) \quad (7)$$

In order to incorporate *both* Rayleigh and the cloud scattering properties, we combine TTHG and Equation 7, by weighting the two phase functions by the fractional opacity of each. In other words, if τ_{cld} is the contribution of scattering from clouds, τ_{ray} is the contribution

Key	Formalism	Inputs Required	Pro/Con
OTHG	Eqn. 3	g	Does not capture back scattering.
TTHG	Eqn. 5	g_f, g_b, c_1, c_2, c_3	Captures small back peak.
TTHG_Ray ^a	Eqn. 8	$g_f, g_b, c_1, c_2, c_3, \tau_{ray}, \tau_{cld}$	Captures sharper back scattering caused by Rayleigh.

^aPICASO default

Table 1. Single Scattering Options </>

of scattering from Rayleigh, and τ_{scat} is the total scattering, the phase function takes the form:

$$P_{TTHG_ray} = \frac{\tau_{cld}}{\tau_{scat}} P_{TTHG} + \frac{\tau_{ray}}{\tau_{scat}} P_{Ray} \quad (8)$$

This methodology was used in (Feng et al. 2018) and a similar methodology was employed in Cahoy et al. (2010). It is also the default methodology used in PICASO. Table 1 has a full summary of the single scattering methodology.

2.2. Multiple Scattering Component

We cannot use the same forms for phase functions, as we did in §2.1, because the multiple scattering component of the source function (Equation 2) must be integrated over all diffuse angles, μ .

An additional convenience of the HG phase function, is that we can mathematically write it as a series of Legendre polynomials:

$$P_{multi}(\cos \Theta) \approx \sum_{l=0}^{N-1} \beta_l P_l(\cos \Theta) \quad (9)$$

where $P_l(\cos \Theta)$ are the polynomials (not to be confused with another phase function), and β_l are the moments of the phase function. The moments can be written out as:

$$\beta_l = \frac{2l+1}{2} \int_1^{-1} P_l(\cos \Theta) p(\cos \Theta) d \cos \Theta \quad (10)$$

which should look familiar, given the previous equation shown for the asymmetry factor (see Equation 4). Therefore, the moment can just be simplified to $\beta_l = (2l+1)g_l$.

Expanding this polynomial to simply an $N = 1$ expansion gives us:

$$P_{multi}(\cos \Theta) = 1 + 3\bar{g} \cos \Theta = 1 + 3\bar{g}\mu\mu' \quad (11)$$

where an azimuthal independence assumption can reduce $\cos \Theta = \mu\mu'$.

One downfall to this formalism (similar to the OTHG) is that it fails to capture the behavior of Rayleigh scattering (as \bar{g} is zero for Rayleigh). Therefore, many

authors (originating from Snook 1999), have leveraged the fact that the second order Legendre dependence on $\cos^2 \Theta$ is the same as that of Rayleigh (see Equation 7). Therefore, by forcing the second moment $\beta_l = (2l+1)g_l = g_2$ to yield the Rayleigh phase function, we can accurately account for Rayleigh scattering. We set this new parameter, $g_2 = \tau_{ray}/(2\tau_{scat})$, so that when Rayleigh dominates the total opacity, g_2 approaches 1/2, the correct value for Rayleigh (Hansen & Travis 1974).

For multiple scattering, the two options for PICASO are N=1 and N=2 expansions (N=2, being the default). However, we can also add δ -Eddington methodology (explained in the following section) to further improve accuracy.

2.3. δ -Eddington

Low order Legendre expansions are not adequate enough to represent very high forward scattering (which is very asymmetric). Given the high scattering asymmetry produced by Mie scattering particles with sizes larger than typical optical wavelengths (Figure 1), this could be problematic. In order to make lower order approximations more accurate, PICASO leverages the δ -Eddington Approximation (Joseph et al. 1976). In this approximation, \bar{g}, τ, ω (the single scattering albedo) are all scaled by recognizing that a beam which experiences a high degree of forward scattering from high albedo particles essentially still propagates forward with little alteration:

$$g' = \frac{\bar{g}}{1+\bar{g}}, \tau' = \tau(1-\omega\bar{g}^2), \omega' = \frac{\omega(1-\bar{g}^2)}{1-\omega\bar{g}^2} \quad (12)$$

Figure 4 shows a full comparison of all the multiple scattering phase functions. Note, the $N = 2$ expansion with δ -scaling reduces the forward peak to regions where the Legendre polynomials should be in higher agreement with the TTHG (i.e. lower asymmetry).

2.4. Raman Scattering

A small fraction of photons that are scattered via the well-known Rayleigh process, experience a shift to red-der wavelengths caused by the excitation of rotational and vibrations transitions in atmospheric gasses. Although some incident stellar photons are shifted, when

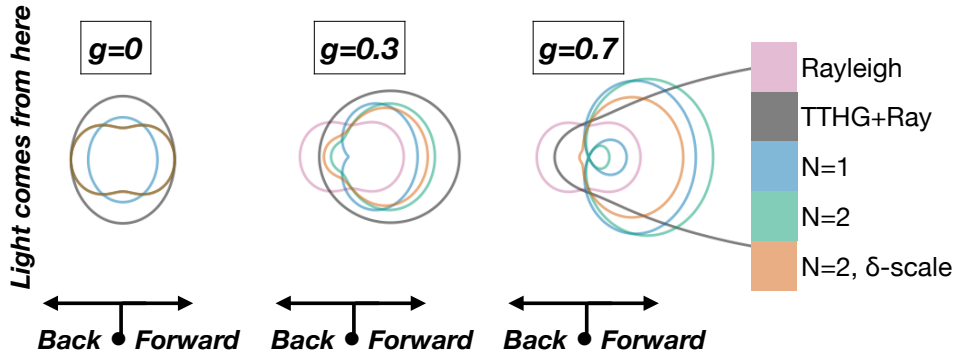


Figure 4. All the options for multiple-scattering phase functions included within PICASO. TTHG with Rayleigh is shown for reference. **Main Point:** As asymmetry increases, approximations to the TTHG phase function get progressively worse. [Q </>](#)

we compute the albedo, we normalize by the original incident flux (see Equation 15). This discrepancy between the shifted incident radiation and the original incident radiation creates new spectral features in the albedo calculation. These detectable shifts are called “ghost” features in the reflected light spectra of planetary atmospheres (Price 1977).

Raman scattering has been detected in the reflected light of all Solar System gas giants (e.g. Karkoschka 1994; Yelle et al. 1987; Courtin 1999). Recently, it was also suggested that Raman scattering could be an important indicator of the main spectroscopic scatterer in the atmospheres of exoplanets, such as H_2 vs. N_2 (Oklopčić et al. 2016). Additionally, it was shown that varying stellar spectra will have a non-negligible affect on the reflected light of exoplanets (Oklopčić et al. 2017).

For the studies of exoplanets, the effect of Raman scattering has been approximated using the methodology of Pollack et al. (1986) (e.g. Marley et al. 1999; Sudarsky et al. 2005; Cahoy et al. 2010). All of these analyses computed Raman scattering correction terms for a 6000 K blackbody. The Pollack et al. (1986) approximation captures the overall shape of Raman scattering by H_2 (i.e. decreased reflectively toward the blue). However, it fails to capture specific ‘ghost’ features from the stellar spectrum at higher resolving powers (as the shift of individual stellar spectral lines are resolved).

For PICASO, we modify the Pollack et al. (1986) approximation to include the Raman cross sections of H_2 computed by Oklopčić et al. (2016). We also retain the original Pollack et al. (1986) methodology, as an option, for low resolution, low SNR observations.

Following Pollack et al. (1986) we introduce the effect of Raman scattering by adding a correction term to the Rayleigh opacity, τ_{Ray} .

$$f_{\text{Ram}} = \frac{\sigma_{\text{Ray}} + \sigma_{\text{Ram}}(f_{\lambda^*}/f_{\lambda})}{\sigma_{\text{Ray}} + \sigma_{\text{Ram}}} \quad (13)$$

where $\sigma_{\text{Ram,Ray}}$ are the cross sections of both Raman and Rayleigh scattering, respectively, and f_{λ}, λ^* are the solar spectra at unshifted, and shifted wavelengths. Each excitation corresponds to a specific wavelength shift of $\lambda^{*-1} = \lambda^{-1} + \Delta\lambda^{-1}$, where $\Delta\lambda$ is the wavelength shift. For reference, the strongest transition of H_2 (the vibrational fundamental) is $\Delta\nu = 4161 \text{ cm}^{-1}$.

Unlike Pollack et al. (1986), we use stellar spectral models from Castelli & Kurucz (2004) for this analysis. PICASO uses PySynphot (STScI Development Team 2013) so that users can draw from different stellar databases.

Additionally, we include initial rotational levels ranging from $J=0$ to $J=9$ for H_2 only since those were the transitions provided by Oklopčić et al. (2016). The cross sections for any given transition from an initial quantum state of $v = 0, J_i$, to final quantum state of v_f, J_f is given by (see Equation A4; Oklopčić et al. (2016)):

$$\sigma_{\text{Ram}}(0, J_i, f_f, J_f, \lambda) = \frac{C}{\lambda^* \lambda^3} [\text{cm}^2] \quad (14)$$

The constant C is given by the values in Table A1 of Oklopčić et al. (2016).

In a future update we will include Raman scattering by N_2 and He but for this work, H_2 is sufficient to study the approximate behavior of Raman scattering.

2.5. Computing Different Types of Albedos

PICASO computes three different kinds of albedos: spherical albedo (A_s), geometric albedo (A_g), and the Bond albedo (A_b). The spherical albedo, A_s , is the fraction of incident light reflected by a sphere towards all angles, and it can be computed for a planet phase geometry, α , by:

$$A_s(\lambda) = 2 \int_0^\pi \frac{F_p(\alpha, \lambda)}{F_{0,L}(\lambda)} \sin \alpha d\alpha \quad (15)$$

where F_p is the emergent flux from the planet, and $F_{0,L}$ is the flux from a perfect Lambert disk under the same

incident flux, F_0 . This spherical albedo, integrated over all angles can be written in two parts: the geometric albedo, and the phase integral. The geometric albedo is just the ratio of the reflected planet flux at full phase, to the incident flux from the perfect Lambert disk:

$$A_g(\lambda) = \frac{F_p(\alpha = 0^\circ, \lambda)}{F_{0,L}(\lambda)}. \quad (16)$$

Then, the phase integral, which is normalized to be 1.0 at full phase, can be written as:

$$q = 2 \int_0^\pi \frac{F_p(\alpha, \lambda)}{F_p(\alpha = 0^\circ, \lambda)} \sin \alpha d\alpha. \quad (17)$$

Although we do not show any Bond albedos here, PICASO does contain the functionality to compute it. The Bond albedo is a stellar flux-weighted reflectivity that is integrated by wavelength:

$$A_b = \frac{\int_0^\infty A_s(\lambda) F_0(\lambda) d\lambda}{\int_0^\infty F_0(\lambda) d\lambda}. \quad (18)$$

Therefore, Bond albedos will vary for two planets that have identical spherical/geometric albedos but orbit different stars (Marley et al. 1999). Since a directly imaged exoplanet will never be observed at full phase, the traditional geometric albedo (which arose from Solar System heritage) can be somewhat cumbersome, given the ratio to the ideal Lambert disk. Nevertheless for ease of comparison with the existing literature we here report results primarily in this framework.

2.6. Planet Phase Geometry

In order to capture phase-dependence, we compute the emergent intensity from the disk at several plane-parallel facets, where each facet has its own incident and outgoing angles. Following Horak & Little (1965), we use a Chebyshev-Gauss integration method to integrate over all the emergent intensities (also used in Cahoy et al. 2010; Madhusudhan & Burrows 2012; Webber et al. 2015). By default, PICASO includes 10 Chebyshev and 10 Gauss angles, which strikes a balance between computational speed and physical accuracy. However this can easily be modified in the code (see options in `justdoit.phase_angle()`). Of course, increasing the number of angles, increases compute time. However, if the user is particularly interested in capturing scattering at high cosine angles (e.g. near the limbs), then it is necessary to increase the number of integration angles accordingly.

Chebyshev-Gauss angles easily translate to planetary latitude and longitude, making it possible to explore the effect of 3D general circulation models on albedo spectra, as in e.g. Webber et al. (2015) and Lee et al. (2017).

Although we do not currently include this in the set of PICASO tutorials, we will make this `jupyter notebook` available soon.

3. AN ANALYSIS OF THE MODELING ASSUMPTIONS

Given our reflected light model, we now aim to determine which modeling assumptions are most important across a large range in parameter space. In particular, we are interested in sampling a parameter space across approximate temperature, cloud properties, and stellar spectrum (to test effects of Raman scattering).

In order to do so, we require, as input, the temperature-pressure profiles, cloud structure, atmospheric composition profile. Batalha et al. (2018b) created a large grid across this particular parameter space. It covered, for a planet with a gravity of 25 m/s², planets with semi-major axes ranging from 0.5-5 AU around a Sun-like star, metallicities (M/H) of 1-100×Solar, and cloud profiles ranging from $f_{\text{sed}} = 0.01 - 6$.

We use these models published in Batalha et al. (2018b) as input. Briefly, the temperature profiles were computed using the radiative-convective model initially developed by McKay et al. (1989) and later updated by Marley & McKay (1999); Marley et al. (2002); Fortney et al. (2005, 2008).

The cloud profiles were computed using a Mie scattering treatment of particle sizes calculated from the model developed by Ackerman & Marley (2001). Each profile was computed using a specific value of f_{sed} , which is used to tune the sedimentation efficiency of the atmosphere. High values of $f_{\text{sed}} > 1$, produce vertically thin clouds with large particles, low values of $f_{\text{sed}} < 1$, produce the opposite—vertically thick clouds with small particles. The Ackerman & Marley (2001) produces, as output: single scattering albedo, cloud extinction, and asymmetry values as a function of atmospheric layer, and wavelength.

The top panel of Figure 5 contains two plots which show the depth in the atmosphere at which the two way optical depth encountered by a photon traversing the atmosphere at $\mu=0.5$ is $\tau = 1$, which we henceforth denote as a *photon attenuation plot*. These two models, chosen from our grid, are computed at 1×Solar with a semi-major axis of 5 AU. The left panel contains a model of a cloud-free system, while the right contains a system with a cloud sedimentation efficiency of $f_{\text{sed}}=3$. We showcase these two case studies throughout the analysis of the modeling assumptions.

The shaded regions of the photon attenuation plot indicate what the dominant source of opacity is as a function of wavelength: molecular absorption (blue), cloud

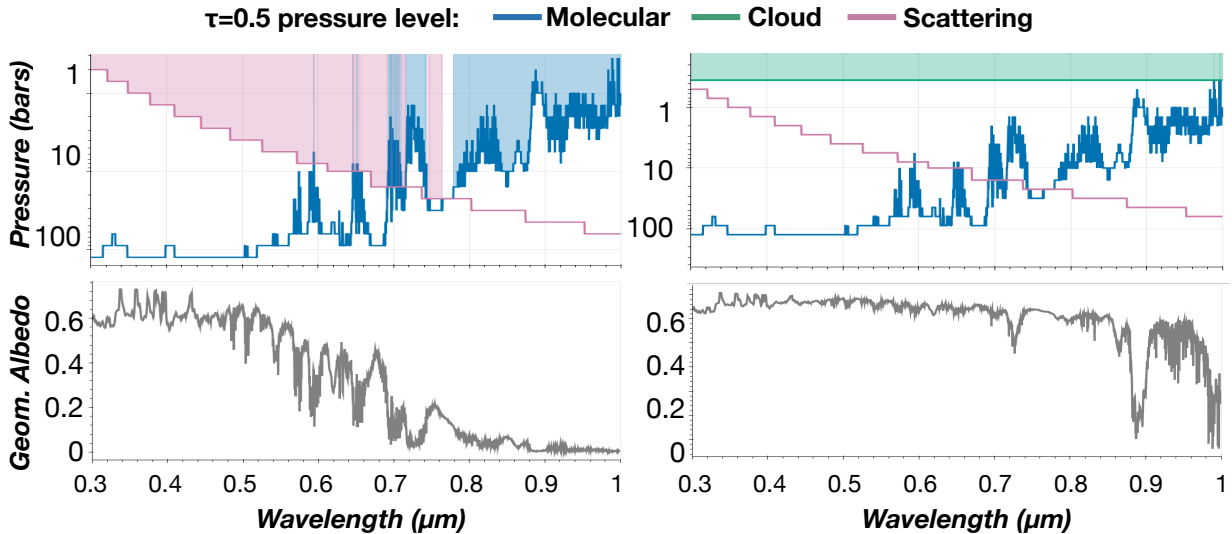


Figure 5. *Photon attenuation plot*, which shows the pressure level at which the two way optical depth encountered by a photon traversing the atmosphere at $\mu = 0.5$ is $\tau = 1$ (top panel). The lower panel shows the corresponding albedo spectra. Each spectrum is computed for a 25 m s^{-2} Jupiter-like planet, 5 AU from a Sun-like star. The left panel is a cloud-free model, while the right panel contains a cloud profile modeled with a sedimentation efficiency of $f_{\text{sed}} = 3$. **Main Point:** Photon attenuation plot shows the dominant source of reflectivity, and therefore can give insight into the overall shape of the reflected light spectrum.

absorption and scattering (green), or Rayleigh scattering (pink). Over the full illuminated hemisphere of a planet the angle of incidence of course varies from $\mu = 0$ to 1 and scattering within cloud decks can increase the effective path length of a photon through the absorbing gas. Thus no single plot can fully capture the complete complexity inherent in the problem, but we find plots such as these helpful for understanding how the shape of reflected light spectra can be traced back to the dominant sources of reflectivity and absorption in the atmosphere. This is especially true for cases where you may have an interplay between the muting of strong scattering features (e.g. Raman) from the presence of optical absorbers (e.g. Na & K).

Indeed such plots are commonly used in Solar System planetary science to help illuminate the relative importance of scattering and absorption at different wavelengths (e.g., [Sromovsky et al. 2009](#)).

3.1. Sensitivity to Single Scattering Phase Function

We first explore the sensitivity of PICASO to the choice in single scattering phase function. Figure 6 shows the same planet case as that in Figure 5. The same spectrum was run using each of the four ways of representing direct scattering in PICASO.

For a cloud-free case where there are no highly asymmetry scatterers, the two TTHG functions and the function used in [Cahoy et al. \(2010\)](#) are all identical (since $g_{\text{cld}} = 0$). However, the cloud-free case shows deviations from the code default (TTHG_ray) on the order of 10-30% when the OTHG phase function is used.

For the cloudy case, Cahoy et al.’s phase function closely matches TTHG_ray, except when Rayleigh scattering opacity is high toward the blue where deviations of $\leq 10\%$ are present. Note all deviations are strongly sensitive to wavelength.

OTHG exhibits the greatest deviation from the other phase functions, because it is not accounting for the back scattering peak from Rayleigh scattering. Figure 2 shows that the Rayleigh contribution as a small back scattering contribution. It is important to note that the actual Rayleigh phase function is symmetric forward and back. But when you combine it with forward scattering particles, the net scattering is more forward.

Even for cases that are seemingly less asymmetric (semi-major axis, $a_s=0.5$ AU, see Figure 1), the specification for direct scattering phase function can still produce spectra that have maximum differences on the order of 100% for full phase observations, and 50% for phase= 90° .

Although we do not show the specific effect of changing, f , the fraction of forward to back scattering, it will also strongly impact the resultant spectrum. Smaller fractions will produce smaller back scattering peaks and yield significantly dimmer spectra across wavelength, and vice versa.

Modeling Recommendation:

- Use default specification for direct scattering (TTHG_Ray)

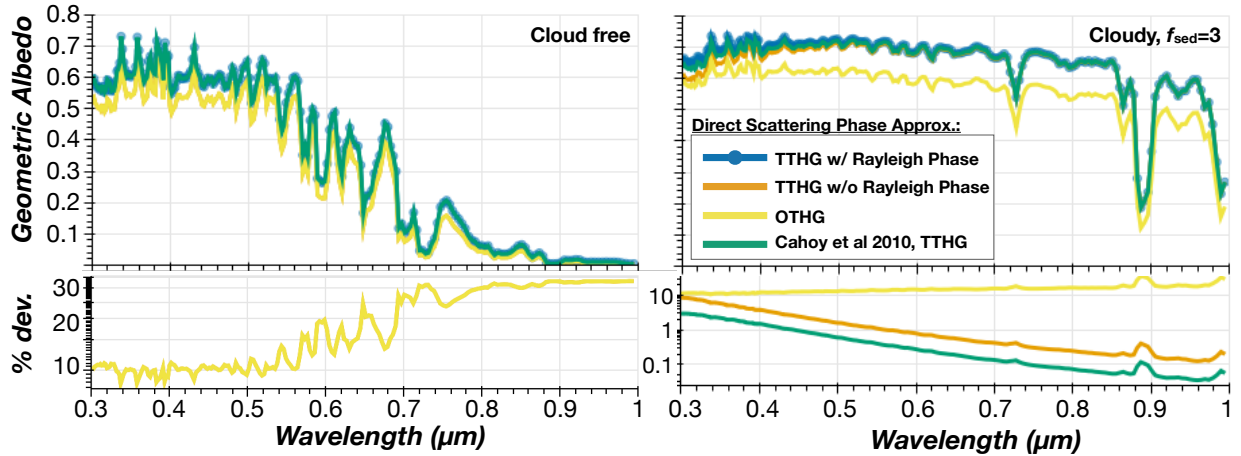


Figure 6. PICASO’s four different methodologies for direct scattering phase functions. All spectra are computed at full phase for a 25m/s^2 Jupiter-like planet 5 Au from a Sun-like star. The left panel is a cloud-free model, while the right panel contains a cloud profile modeled with $f_{sed}=3$. **Main Point:** Assumptions of direct scattering phase function have large effect ($\leq 30\%$) on the resultant spectrum across all wavelengths. [Q](#) [</>](#)

- Fit for the functional form of the fraction, f , of forward to back scattering according to the problem being addressed.

3.2. Multiple Scattering Phase Function & δ -Eddington

Next, we assess PICASO’s sensitivity to the multiple scattering phase function, and the δ -Eddington approximation. Figure 7 shows the modeling sensitivity to the user’s choice for multiple scattering phase function. For both cloud-free and cloudy cases, there are $\leq 1\%$ differences when choosing between a $N = 1$ or $N = 2$ Legendre expansion. The $N = 2$ expansion is used to approximate the multiple scattering by Rayleigh scattering. Therefore, for the cases modeled here, the diffuse scattering by Rayleigh is a relatively small contribution to the total reflectivity. As observations increase in precision we will have to revisit whether or not this holds true. Studies of the accuracy of Legendre polynomial expansions suggest that they made degrade in accuracy for asymmetric large particles (Zhang et al. 2017). Zhang et al. (2017) also suggested that Chebyshev polynomial expansions as a more accurate alternative. We will save this for a future update, when better data warrant higher accuracy phase functions.

In order to improve the parameterization of these expansions, PICASO leverages the δ -Eddington method of scaling the single scattering albedo, opacity, and asymmetry parameter. When g_{cld} is nonzero, choice of the δ -Eddington method impacts the spectra by up to 30% in some cases. We set $N = 2$ δ -Eddington as default since it can reproduce, with relatively high accuracy, observations of Earth (Feng et al. 2018), and Jupiter (Cahoy et al. 2010).

As more diverse populations of exoplanets are observed in reflected light with higher signal-to-noise ratio (SNR), we will conduct a more thorough investigation of these approximations. Since the publication of the δ -Eddington method (Joseph et al. 1976), several other techniques have also been developed to improve the phase function parameterization (e.g. Hu et al. 2000; Iwabuchi & Suzuki 2009; Sorensen et al. 2017). We will consider these in a future update.

Modeling Recommendation: For planet cases with some degree of asymmetric cloud scatterers, always use $N=2$ Legendre polynomial expansion with the δ -Eddington correction.

3.3. Raman Scattering

Figure 8 shows the modeling sensitivity to PICASO’s two methodologies for computing Raman scattering. The Pollack et al. (1986) approximation captures the general behavior of the decline in reflectivity toward the blue, but fails to produce any spectral features. When the Pollack et al. approximation is modified to include cross sections computed from Oklopčić et al. (2016), ghost spectral features are introduced at the $\sim 10\%$ level. Spectral features begin to disappear at $R \sim 50$, but small 1% baseline differences still remain at $R \sim 10$.

For a $T_{\text{eff}}=6000$ K star (the Pollack et al. default), 10% differences remain through $0.55\mu\text{m}$ (after the Mg I feature at 5200\AA). Cooler stars (toward $T_{\text{eff}}=2600$ K), with more crowded molecular features, create spectral differences out past $0.65\mu\text{m}$. Cloudy spectra (e.g. Figure 4 right panel) are also sensitive to Raman scattering features despite the prominent cloud opacity in the blue.

Differences between the calculations here and those shown in Oklopčić et al. (2017) (see Figure 4) and Sro-

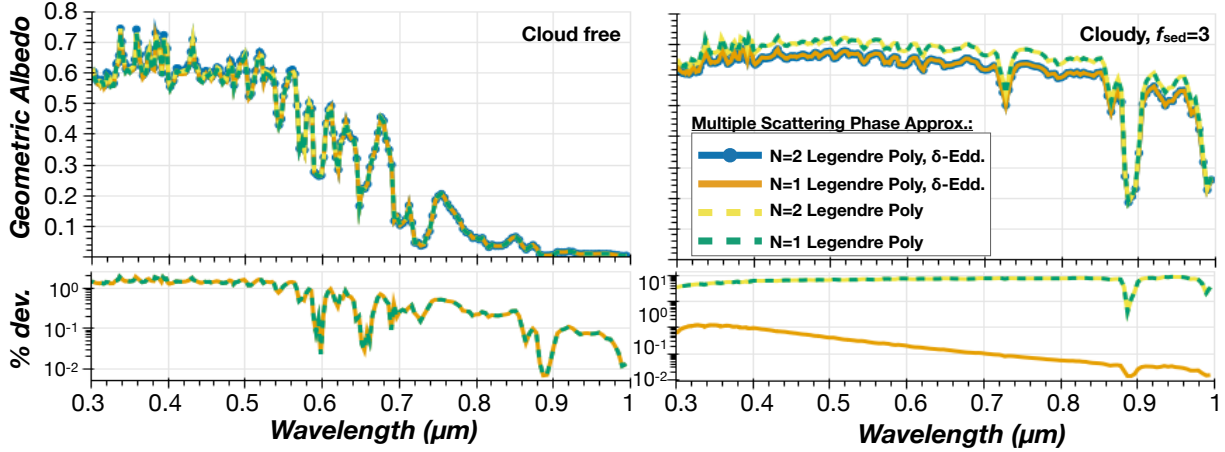


Figure 7. Spectra and percent deviation between the code default and all other PICASO specifications for phase function. Planet cases are identical to those shown in Figure 6. **Main Point:** Use of δ -Eddington approximation has largest impact on spectra. [Q](#) [</>](#)

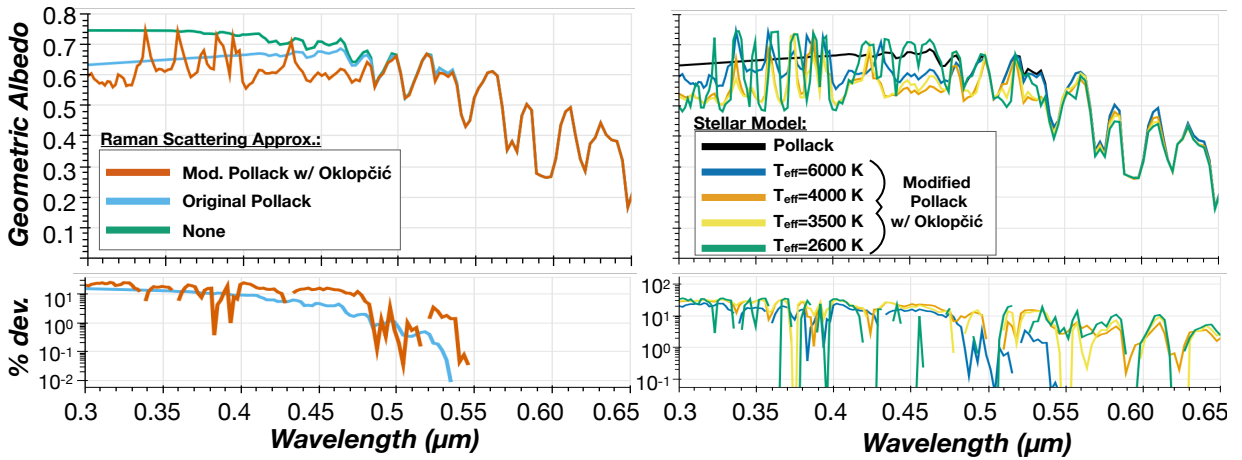


Figure 8. Spectra and percent deviation between the code default and all other PICASO specifications for phase function. Planet cases are identical to those shown in Figure 6. **Main Point:** Even at low resolution ($R=100$), Raman scattering is important to include, especially for cool stars. [Q](#) [</>](#)

movsky (2005) (see Figure 17) are attributed to the resolution of the stellar spectrum, and the stellar databases chosen. A key input to modeling Raman scattering correctly is an accurate, high-resolution stellar spectrum. Oklopčić et al. (2017) used stellar spectra from Valdes et al. (2004) database, which are computed with $\Delta\lambda=1 \text{ \AA}$. Sromovsky (2005) used a Solar spectrum from the Upper Atmospheric Research Satellite, which had a nominal resolution of 2 \AA . The Castelli & Kurucz (2004) grid used here is computed at a resolution of 10 \AA . This lower resolution grid will result in an under estimation of the Raman effect. One additional, minor, difference can be seen in the $T_{eff}=2600 \text{ K}$ spectrum. Around $0.35 \mu\text{m}$, some spectral features appear to have flat tops. This is a result, originally pointed out in Courtin (1999), of instabilities in the solution of the radiative transfer

equation that prevent us from allowing Equation 13 to be greater than 1. Despite these differences, our modified Pollack approximation is a much more accurate solution than the original Pollack methodology.

One last subtlety is that Figure 8 makes it seem as if Raman scattering has a dramatic effect on the total energy of budget of the atmosphere. This is somewhat exaggerated by the way in which the albedo is defined, by ratioing to the stellar flux. It has to be accounted for in order for the ratio to be correct, but in actuality is not a huge influence on the energy budget of the atmosphere. The effect of the small deposition of energy into the atmosphere by the small wavelength shifts that occur for those photons that experience this form of scattering would have to be computed by a complete radiative-convective equilibrium code which carefully tracks the

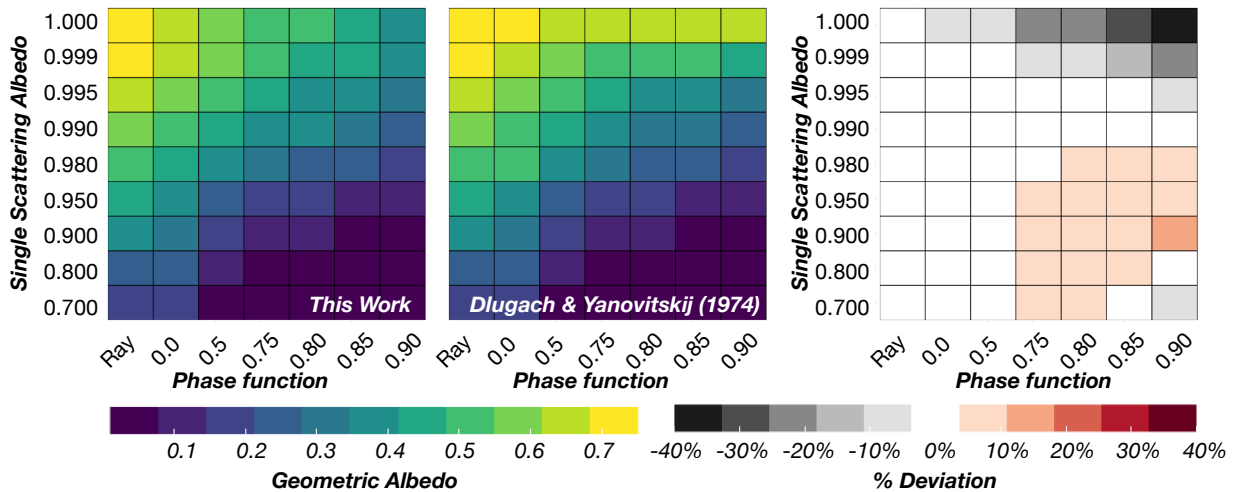


Figure 9. A summary of the benchmark analysis between [Dlugach & Yanovitskij \(1974\)](#) and this work. Left two panels shows the geometric albedo for a range of single scattering albedos and phase functions. Right-most plot shows the difference map between the two. **Main Point:** Models agree within 10% for most cases, with a maximum discrepancy of 40% for highly asymmetric cases.

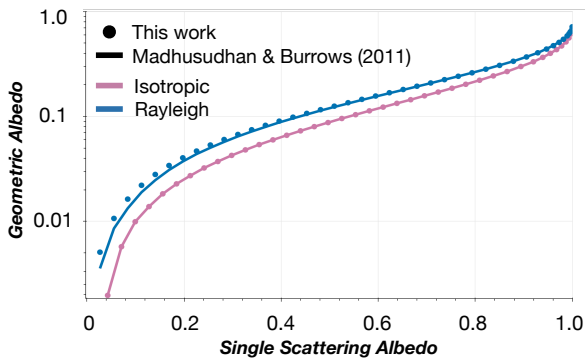


Figure 10. Summary of the benchmark analysis between [Madhusudhan & Burrows \(2012\)](#) and this work. The greatest divergence occurs at very low geometric albedo (≤ 0.1). **Main Point:** Overall, models agree within 10% in all isotropic and rayleigh phase functions cases.

energy budget of the atmosphere. Since PICASO is focused on tracking the reflectivity of the atmosphere as a whole it is not well suited to this particular task and doing so is beyond the scope of this paper.

Modeling Recommendation: Choose Pollack et al. methodology with [Oklopčić et al. \(2016\)](#) cross sections, and choose a stellar spectrum that matches the level of resolution and accuracy needed.

4. BENCHMARK ANALYSIS

In order to benchmark the accuracy of the code, we chose to compare against the results of [Dlugach & Yanovitskij \(1974\)](#) and [Madhusudhan & Burrows \(2012\)](#). [Dlugach & Yanovitskij \(1974\)](#) computed the intensity of radiation diffusely reflected from a semi-infinite homogeneous atmosphere with arbitrary single scattering phase function. Their analysis focused on

the optical properties of Venus and the Jovian planets. Therefore, they carried out calculations for Rayleigh and the HG phase functions with asymmetry parameters ranging from 0-0.9, and single scattering albedos ranging from 0.7-1. [Madhusudhan & Burrows \(2012\)](#) provided analytic phase expressions for geometric albedo as a function of single scattering albedo for both Rayleigh scattering and isotropy in a semi-infinite atmosphere. We compare PICASO against two models (one originating from Solar System science, the other originating from exoplanet science) across a wide range in phase function, and single scattering albedo is sufficient enough to prove accuracy of the model.

Figure 9 shows the first comparison against [Dlugach & Yanovitskij \(1974\)](#). [Dlugach et al.](#) used a one-term HG phase function for all asymmetric calculations. Therefore, it is important to note that if comparisons are carried out using PICASO’s default (as opposed to using OTHG for the single scattering phase function), the results will not agree well. This further motivates our choice for inheriting older methodologies of computing phase functions so that fruitful code comparisons are easily accessible.

Using a OTHG phase function, the models agree within 10% for all Rayleigh phase functions and for $g \leq 0.5$. The models start to exhibit 10% differences for $0.5 < g \leq 0.85$. Since the diversity of cases illustrated in Figure 1 fall in this range of asymmetry values, we feel that this can be considered in good agreement. There are few cases with $g = 0.9$ that exhibit $\sim 40\%$ differences. However, it is not obvious what these differences could be attributed to. [Dlugach & Yanovitskij \(1974\)](#) computes higher geometric albedos when single scatter-

ing is less than 0.98, and lower geometric albedos when single scattering is ~ 1 . Given the complete independence of the two models, there are numerous factors that could potentially contribute to this including: the diffuse scattering calculation, geometric integration, radiative transfer solver. Because majority of cases fall within 10% agreement we consider these two models to be in good agreement.

Figure 10 shows the comparison between the calculations in Madhusudhan & Burrows (2012) and PICASO. Here, we only compare isotropic and Rayleigh cases across a range of single scattering albedos. Our results are well within 10% agreement. The largest deviation comes from the computation of very low geometric albedos (~ 0.01). Such very low single scattering albedos are well outside the range expected for the types of clouds expected (Figure 1), although unusual composition particles (e.g., Gao et al. (2017)) can be quite dark at some wavelengths. We consider PICASO and the analytic model of Madhusudhan & Burrows (2012) to be in good agreement.

5. INFORMATION CONTENT ANALYSIS OF REFLECTED LIGHT

Currently, an important driver for the creation of PICASO is to determine optimal observing strategies for future direct imaging missions, such as *WFIRST*, ELTs, and potential large space based observatories such as LUVOIR or HabEx. For example, determining band pass ranges, minimum SNR, and instrument resolving powers that maximize the total retrievable information from a planetary reflected light spectrum will be a critical contribution to the design of future facilities. Throughout this analysis, we focus specifically on the approximate SNR, bandpass, and resolution of the *WFIRST*-Coronagraphic Instrument, which is a technology demonstrator for future concept mission like LUVOIR or HabEx. Our methodology, though, can be applied to any parameter space.

Lupu et al. (2016) and Nayak et al. (2017) began to explore optimal observing strategies by wrapping the original Fortran code outlined in Cahoy et al. (2010) and others, in a sophisticated retrieval framework. Lupu et al. (2016) focused on our ability to ascertain the presence or absence of clouds and CH_4 , while Nayak et al. (2017) focused on our ability to constrain planet phase and radius. These studies offered valuable insights into our ability to constrain the atmospheres of exoplanets with reflected light. However, the computational limitations of MCMC (or similar) methods hinders our ability to rapidly move through a large parameter space in atmospheric diversity, resolution, and SNR.

Information content (IC) theory offers an alternative to full MCMC methods. IC has been commonly used in Earth and Solar System science (e.g. Kuai et al. 2010; Saitoh et al. 2009), as well as in exoplanet science (e.g. Line et al. 2012; Batalha & Line 2017; Howe et al. 2017; Batalha et al. 2018a). We use the IC model originally developed for transiting exoplanet science. A full description of the methodology can be found in Batalha & Line (2017).

IC theory relies heavily on computing the Jacobian of individual systems, which describe how sensitive the model is to slight perturbations of the state vector parameters at a given initial state. In this analysis we assume that the state vector is made up of $[T(P), \xi_i, g]$, where $T(P)$ is the pressure-dependent temperature profile, ξ_i is the mixing ratio of species i , and g is the gravity. We compute the derivative of the Jacobian using a centered-finite difference scheme. Our $T(P)$ and mixing ratio profiles come from the calculations in Batalha et al. (2018b), so that perturbations shift the entire profile. $T(P)$ and g are perturbed linearly, with 0.1% perturbations. ξ_i 's are perturbed in log space, also with 0.1% perturbations. These finite perturbations were chosen to reproduce the results of a full retrieval analyses.

Of course there are several other parameters that contribute to an atmospheric state. Choosing only $T(P)$, ξ_i , g is almost certainly too simplistic. For example, as we've seen here, the cloud asymmetry parameter and the single scattering albedo will largely contribute to how well we can constrain the atmospheres of exoplanets. Additionally, Lupu et al. (2016) showed that the pressure of the cloud deck will also influence the shape of the spectral features. In order to capture this behavior, we compute the Jacobian across a diversity of initial states ($a_s=0.5-5.0$ AU, $f_{\text{sed}}=0.1-6$) at a phase angle of 90° . As shown in Figure 1, this covers a broad diversity of cases in single scattering and asymmetry, to compensate for our simplistic state vector.

Along with the Jacobian, \mathbf{K} , we also need an approximation of the error covariance, \mathbf{S}_e , and \mathbf{S}_a , the *a priori* covariance matrix. We take the values of the error covariance matrix from the cases in Nayak et al. (2017) for SNR=5-25. The priors, \mathbf{S}_a , represents the information we start with for any given system. We assume broad uniform priors for every state vector parameter. In other words, we assume to have very little information about the system before conducting our observation: ± 300 K for $T(P)$, ± 6 dex for mixing ratio, $\pm 100\text{m/s}^2$ for gravity. Given \mathbf{K} , \mathbf{S}_e , and \mathbf{S}_a , we can compute the posterior covariance matrix, which gives the 1-sigma uncertainty on a state vector parameter after a measurement is made:

$$\hat{\mathbf{S}} = (\mathbf{K}^T \mathbf{S}_e^{-1} \mathbf{K} + \mathbf{S}_a^{-1})^{-1} \quad (19)$$

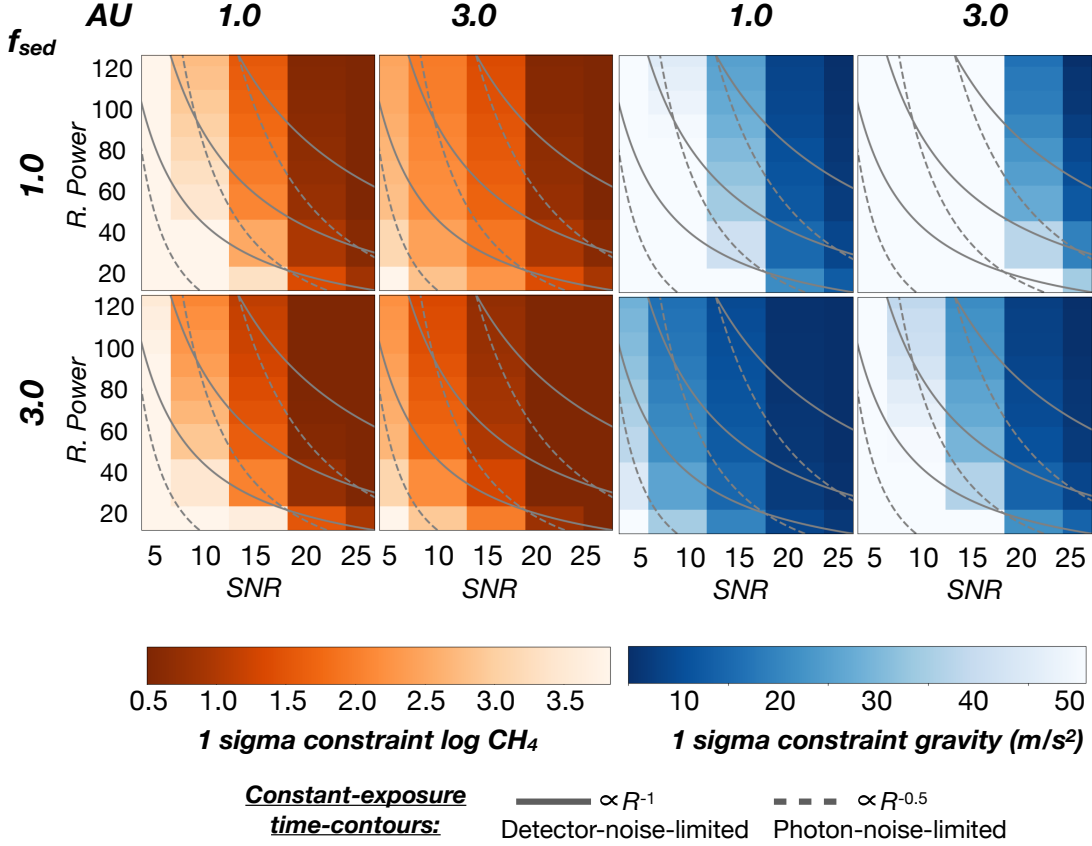


Figure 11. Information content analysis for a subset of the full parameter space covered here. In all plots, darker colors correspond to tighter constrained planetary systems. All spectra simulations were computed for a $1\times$ Solar, 25m/s^2 planet, around a Sun-like star. The approximate *WFIRST* wavelength range of $0.5\text{-}0.76\mu\text{m}$ was used with the SNR calculations computed in [Nayak et al. \(2017\)](#). Due to the assumption of chemical equilibrium, the main absorber in all models shown is CH_4 . On each subplot we show constant exposure-time contours for detector-noise-limited and photon-noise-limited observations. **Main Point:** We need $\text{SNR}=20$ to *constrain* composition and gravity. Results are less sensitive to resolving power.

Because of the \mathbf{S}_a^{-1} dependence, using large priors guarantees that our estimates for the posterior covariance matrix are solely driven by the model sensitivity (via the Jacobian) and the expected data quality at each wavelength (e.g. $\mathbf{K}^T \mathbf{S}_e^{-1} \mathbf{K} \gg \mathbf{S}_a^{-1}$). Additionally, we spot checked our analysis against the full retrievals done in [Lupu et al. \(2016\)](#) & [Nayak et al. \(2017\)](#), and found that they are in good agreement.

Figure 11 shows a summary of the results of the IC analysis for a subset of a_s and f_{sed} . We focus on this subset because it is the “sweet spot” in parameter space for a *WFIRST*-CGI mission. However, we discuss the full parameter space in §5.1 & §5.2. Additionally, Figure 11 shows constant exposure time contours for both detector-noise and photon-limited observations. Because *WFIRST* instrumentation has not yet been finalized, we cannot add definitive exposure times on each of these curves. However, we include them anyways to give readers an understanding of the SNR-Resolving Power interplay, in terms of total time (e.g. for detector-

noise limited observations it takes equal time to achieve $\text{SNR}=25$ at $R=40$, as $\text{SNR}=5$ at $R=120$). As *WFIRST* instrumentation is solidified, we will perform more robust noise simulations with estimates for integration time.

Overall, our ability to constrain composition and gravity are more dependent on the SNR, as opposed to instrument resolving power. Regardless of resolving power, $\text{SNR}=10$ is not sufficient to *constrain* either composition or gravity (our definition of constraint is discussed in the following §5.1). Generally, a $\text{SNR}\sim 20$ is needed to attain robust constraints on composition and gravity.

5.1. Sensitivity to Composition

Figure 11 only shows the ability to constrain the abundance of CH_4 , the dominant absorber at these temperatures. From $a_s=0.5\text{-}5$, there is a transition from alkali-dominated atmospheres (Na & K) toward 0.5 AU, to CH_4 -dominated atmospheres toward 5 AU. This transition, a result of chemical equilibrium, roughly occurs at

0.85 AU (see Batalha et al. 2018b), where both alkali and CH₄ features are comparatively small. *WFIRST-CGI*, with a proposed wavelength coverage for spectroscopy of $\sim 0.6\text{--}0.76\ \mu\text{m}$ will be primarily focused on the detection of CH₄. Therefore, we only show figures for $a_s = 1$ & 3 AU because most of the considered targets will fall in this range.

At SNR=5, constraints on CH₄ approach the prior value, meaning the observation does not contribute to the overall knowledge. A definition of “good” constraint is relatively arbitrary, but adopt the definition of Feng et al. (2018), which is effectively the ability to constrain the abundance within ± 1.0 log units. Although, this may seem too stringent a definition, IC analyses tends to be more optimistic than full retrieval analyses. This is because IC cannot pick up on important factors such as degeneracies between state vector parameters.

The difference in being able to detect CH₄ at 1 AU versus 3 AU comes from the relative size of the molecular features, and the cloud composition. At 1 AU, even though Na & K are nearly gone, CH₄ is still not as pronounced as it is at 3 AU, because the volume mixing ratio is lower. Additionally, higher-in-altitude water clouds will weaken the feature.

The cloud parameter f_{sed} appears to have a lesser effect than semi-major axis. This is because at moderately high values of f_{sed} , the cloud deck is at low enough pressures as to not completely impede the detection of molecular features. For $f_{\text{sed}} \leq 1$, detection of CH₄ (or any other molecular feature) will be difficult to impossible because the path length for reflected light through the atmosphere is too short.

5.2. Sensitivity to Gravity

The effect of gravity on reflected light is summarized in Figure 3 & 4 in Lupu et al. (2016). Generally, increasing gravity increases the depth of spectral features and increases reflectively towards the blue. There is also a more subtle effect of gravity on the $0.8\ \mu\text{m}$ H₂ continuum feature (at lower gravity the feature is stronger). We are not able to leverage this effect because of *WFIRST-CGI*’s spectroscopic wavelength coverage.

For SNR ≤ 10 the constraint on gravity, approaches the prior, meaning the observation does yet not contribute to the overall knowledge. It also appears that 1 AU systems are slightly more amenable to gravity characterization as opposed to 3 AU. This because at 3 AU when $f_{\text{sed}} \geq 1$, water cloud reflectively dominates the opacity, as opposed to at 1 AU, where there is still a contribution from scattering by Rayleigh. When water cloud opacity dominates the opacity, the spectrum is less sensitive to slight perturbations in gravity. This

is also why the $f_{\text{sed}}=3$ cases are better constrained, as opposed to the $f_{\text{sed}}=1$ cases.

6. DISCUSSION & CONCLUSION

Here, we presented an initial release of a reflected light code, called PICASO. PICASO is versatile enough for calculations of reflected light spectroscopy, and for retrievals of directly imaged exoplanet atmospheres. It has been benchmarked against two independent codes from Dlugach & Yanovitskij (1974) and Madhusudhan & Burrows (2012). For isotropic and Rayleigh scattering, PICASO agrees with other codes to well within 10%. For asymmetric scattering, calculations are slightly more discrepant, but well within the bounds of observational precision ($\sim 10\%$ agreement).

PICASO contains several methodologies for computing calculations of reflected light. Specifically, we have focused on highlighting different methodologies for computing single scattering, multiple scattering, and Raman scattering. Within each section, we have provided recommendations for modeling exoplanets, which are also PICASO’s default run settings. A further explanation of this is available in our online radiative transfer tutorial⁴.

Our information content analysis demonstrates the approximate parameter space in cloud composition, resolving power, and SNR, where we can expect to get robust constraints on composition and gravity. We find that in general, we need an SNR ~ 20 to attain constraints on composition, where our definition for constraint is attaining a $1\text{-}\sigma$ confidence interval of ± 1 log unit on the volume mixing ratio of the dominant absorber (following Feng et al. 2018).

Despite the versatility of the original release, there are still aspects which we are currently working on. Future releases of the code will contain:

1. Thermal Emission
2. δ -M stream method (Wiscombe 1977)
3. Raman scattering by N₂ and He
4. Chebyshev polynomial for multiple scattering phase function
5. Compatibility with nested sampling algorithm

Additionally, a robust retrieval analysis will be needed to address degeneracies that cannot be captured in an information content analysis. This includes developing methods to constrain radius, directly retrieve the optical properties of the clouds (i.e. the imaginary component of the refractive index), and discern the presence

⁴ [Q:Physics Tutorial](#)

of photochemical hazes. This analysis will additionally be added as a future code release since PICASO contains the modularity and versatility to support it.

We thank Kerri Cahoy for helpful discussion and tracking down various versions of the original albedo code. Additionally, we thank Cornell undergraduate Mark Siebert, and Caltech graduate student Danica Adams for being the first beta testers, and pointing out some bugs in the code and installation. N.E.B acknowledges support from the University of California

Presidents Postdoctoral Fellowship Program. M.S.M. acknowledges support from GSFSC Sellers Exoplanet Environments Collaboration (SEEC), with funding specifically by the NASA Astrophysics Divisions Internal Scientist Funding Model.

Software: numba (Lam et al. 2015), pandas (McKinney 2010), bokeh (Bokeh Development Team 2014), NumPy (Walt et al. 2011), IPython (Pérez & Granger 2007), Jupyter, (Kluyver et al. 2016), PySynphot (STScI Development Team 2013), sqlite3 (sqlite3 Development Team 2019), picaso (Batalha 2019)

REFERENCES

- Ackerman, A. S., & Marley, M. S. 2001, *ApJ*, 556, 872, doi: [10.1086/321540](https://doi.org/10.1086/321540)
- Barstow, J. K., Aigrain, S., Irwin, P. G. J., et al. 2014, *ApJ*, 786, 154, doi: [10.1088/0004-637X/786/2/154](https://doi.org/10.1088/0004-637X/786/2/154)
- Barstow, J. K., Aigrain, S., Irwin, P. G. J., & Sing, D. K. 2017, *ApJ*, 834, 50, doi: [10.3847/1538-4357/834/1/50](https://doi.org/10.3847/1538-4357/834/1/50)
- Batalha, N. 2019, natashabatalha/picaso: Initial Publication Release, doi: [10.5281/zenodo.2647593](https://doi.org/10.5281/zenodo.2647593), <https://doi.org/10.5281/zenodo.2647593>
- Batalha, N. E., Lewis, N. K., Line, M. R., Valenti, J., & Stevenson, K. 2018a, *ApJL*, 856, L34, doi: [10.3847/2041-8213/aab896](https://doi.org/10.3847/2041-8213/aab896)
- Batalha, N. E., & Line, M. R. 2017, *AJ*, 153, 151, doi: [10.3847/1538-3881/aa5faa](https://doi.org/10.3847/1538-3881/aa5faa)
- Batalha, N. E., Smith, A. J. R. W., Lewis, N. K., et al. 2018b, *AJ*, 156, 158, doi: [10.3847/1538-3881/aad59d](https://doi.org/10.3847/1538-3881/aad59d)
- . 2018c, Color Classification of Extrasolar Giant Planets: Prospects and Cautions, doi: [10.5281/zenodo.2003949](https://doi.org/10.5281/zenodo.2003949), <https://doi.org/10.5281/zenodo.2003949>
- Baudino, J.-L., Mollière, P., Venot, O., et al. 2017, *ApJ*, 850, 150, doi: [10.3847/1538-4357/aa95be](https://doi.org/10.3847/1538-4357/aa95be)
- Benneke, B., & Seager, S. 2012, *ApJ*, 753, 100, doi: [10.1088/0004-637X/753/2/100](https://doi.org/10.1088/0004-637X/753/2/100)
- Bokeh Development Team. 2014, Bokeh: Python library for interactive visualization
- Cahoy, K. L., Marley, M. S., & Fortney, J. J. 2010, *ApJ*, 724, 189, doi: [10.1088/0004-637X/724/1/189](https://doi.org/10.1088/0004-637X/724/1/189)
- Castelli, F., & Kurucz, R. L. 2004, arXiv Astrophysics e-prints
- Courtin, R. 1999, *Planet. Space Sci.*, 47, 1077, doi: [10.1016/S0032-0633\(99\)00013-6](https://doi.org/10.1016/S0032-0633(99)00013-6)
- Demory, B.-O., de Wit, J., Lewis, N., et al. 2013, *ApJL*, 776, L25, doi: [10.1088/2041-8205/776/2/L25](https://doi.org/10.1088/2041-8205/776/2/L25)
- Dlugach, J. M., & Yanovitskij, E. G. 1974, *Icarus*, 22, 66, doi: [10.1016/0019-1035\(74\)90167-5](https://doi.org/10.1016/0019-1035(74)90167-5)
- Dyudina, U., Zhang, X., Li, L., et al. 2016, *ApJ*, 822, 76, doi: [10.3847/0004-637X/822/2/76](https://doi.org/10.3847/0004-637X/822/2/76)
- Esteves, L. J., De Mooij, E. J. W., & Jayawardhana, R. 2015, *ApJ*, 804, 150, doi: [10.1088/0004-637X/804/2/150](https://doi.org/10.1088/0004-637X/804/2/150)
- Evans, T. M., Pont, F., Sing, D. K., et al. 2013, *ApJL*, 772, L16, doi: [10.1088/2041-8205/772/2/L16](https://doi.org/10.1088/2041-8205/772/2/L16)
- Feng, Y. K., Robinson, T. D., Fortney, J. J., et al. 2018, *AJ*, 155, 200, doi: [10.3847/1538-3881/aab95c](https://doi.org/10.3847/1538-3881/aab95c)
- Fortney, J. J., Lodders, K., Marley, M. S., & Freedman, R. S. 2008, *ApJ*, 678, 1419, doi: [10.1086/528370](https://doi.org/10.1086/528370)
- Fortney, J. J., Marley, M. S., Lodders, K., Saumon, D., & Freedman, R. 2005, *ApJL*, 627, L69, doi: [10.1086/431952](https://doi.org/10.1086/431952)
- Freedman, R. S., Marley, M. S., & Lodders, K. 2008, *ApJS*, 174, 504, doi: [10.1086/521793](https://doi.org/10.1086/521793)
- Gao, P., Marley, M. S., Zahnle, K., Robinson, T. D., & Lewis, N. K. 2017, *AJ*, 153, 139, doi: [10.3847/1538-3881/aa5fab](https://doi.org/10.3847/1538-3881/aa5fab)
- Garcia Munoz, A., & Isaak, K. G. 2015, Proceedings of the National Academy of Science, 112, 13461, doi: [10.1073/pnas.1509135112](https://doi.org/10.1073/pnas.1509135112)
- Goody, R. M., & Yung, Y. L. 1989, Atmospheric radiation : theoretical basis
- Hansen, J. E. 1969, *Journal of Atmospheric Sciences*, 26, 478, doi: [10.1175/1520-0469\(1969\)026<0478:EAASFM>2.0.CO;2](https://doi.org/10.1175/1520-0469(1969)026<0478:EAASFM>2.0.CO;2)
- Hansen, J. E., & Travis, L. D. 1974, *SSRv*, 16, 527, doi: [10.1007/BF00168069](https://doi.org/10.1007/BF00168069)
- Horak, H. G., & Little, S. J. 1965, *ApJS*, 11, 373, doi: [10.1086/190119](https://doi.org/10.1086/190119)
- Howe, A. R., Burrows, A., & Deming, D. 2017, *ApJ*, 835, 96, doi: [10.3847/1538-4357/835/1/96](https://doi.org/10.3847/1538-4357/835/1/96)
- Hu, Y.-X., Wielicki, B., Lin, B., et al. 2000, *Journal of Quantitative Spectroscopy and Radiative Transfer*, 65, 681
- Irwin, P. G. J., Bowles, N., Braude, A. S., et al. 2019a, *Icarus*, 321, 572, doi: [10.1016/j.icarus.2018.12.008](https://doi.org/10.1016/j.icarus.2018.12.008)

- Irwin, P. G. J., Toledo, D., Garland, R., et al. 2019b, *Icarus*, 321, 550, doi: [10.1016/j.icarus.2018.12.014](https://doi.org/10.1016/j.icarus.2018.12.014)
- Irwin, P. G. J., Teanby, N. A., de Kok, R., et al. 2008, *JQSRT*, 109, 1136, doi: [10.1016/j.jqsrt.2007.11.006](https://doi.org/10.1016/j.jqsrt.2007.11.006)
- Iwabuchi, H., & Suzuki, T. 2009, *Journal of Quantitative Spectroscopy and Radiative Transfer*, 110, 1926
- Joseph, J. H., Wiscombe, W. J., & Weinman, J. A. 1976, *Journal of Atmospheric Sciences*, 33, 2452, doi: [10.1175/1520-0469\(1976\)033<2452:TDEAFR>2.0.CO;2](https://doi.org/10.1175/1520-0469(1976)033<2452:TDEAFR>2.0.CO;2)
- Karkoschka, E. 1994, *Icarus*, 111, 174, doi: [10.1006/icar.1994.1139](https://doi.org/10.1006/icar.1994.1139)
- Kluyver, T., Ragan-Kelley, B., Pérez, F., et al. 2016, in *ELPUB*, 87–90
- Kuai, L., Natraj, V., Shia, R.-L., Miller, C., & Yung, Y. L. 2010, *JQSRT*, 111, 1296, doi: [10.1016/j.jqsrt.2010.02.011](https://doi.org/10.1016/j.jqsrt.2010.02.011)
- Lacy, B., Shlivko, D., & Burrows, A. 2019, *AJ*, 157, 132, doi: [10.3847/1538-3881/ab0415](https://doi.org/10.3847/1538-3881/ab0415)
- Lam, S. K., Pitrou, A., & Seibert, S. 2015, in *Proceedings of the Second Workshop on the LLVM Compiler Infrastructure in HPC, LLVM '15 (New York, NY, USA: ACM)*, 7:1–7:6. <http://doi.acm.org/10.1145/2833157.2833162>
- Lee, G. K. H., Wood, K., Dobbs-Dixon, I., Rice, A., & Helling, C. 2017, *A&A*, 601, A22, doi: [10.1051/0004-6361/201629804](https://doi.org/10.1051/0004-6361/201629804)
- Line, M. R., Zhang, X., Vasisht, G., et al. 2012, *ApJ*, 749, 93, doi: [10.1088/0004-637X/749/1/93](https://doi.org/10.1088/0004-637X/749/1/93)
- Lupu, R. E., Marley, M. S., Lewis, N., et al. 2016, *AJ*, 152, 217, doi: [10.3847/0004-6256/152/6/217](https://doi.org/10.3847/0004-6256/152/6/217)
- MacDonald, R. J., Marley, M. S., Fortney, J. J., & Lewis, N. K. 2018, *ApJ*, 858, 69, doi: [10.3847/1538-4357/aabb05](https://doi.org/10.3847/1538-4357/aabb05)
- Madhusudhan, N., & Burrows, A. 2012, *ApJ*, 747, 25, doi: [10.1088/0004-637X/747/1/25](https://doi.org/10.1088/0004-637X/747/1/25)
- Madhusudhan, N., & Seager, S. 2009, *ApJ*, 707, 24, doi: [10.1088/0004-637X/707/1/24](https://doi.org/10.1088/0004-637X/707/1/24)
- Marley, M. S., Gelino, C., Stephens, D., Lunine, J. I., & Freedman, R. 1999, *ApJ*, 513, 879, doi: [10.1086/306881](https://doi.org/10.1086/306881)
- Marley, M. S., & McKay, C. P. 1999, *Icarus*, 138, 268, doi: [10.1006/icar.1998.6071](https://doi.org/10.1006/icar.1998.6071)
- Marley, M. S., Seager, S., Saumon, D., et al. 2002, *ApJ*, 568, 335, doi: [10.1086/338800](https://doi.org/10.1086/338800)
- McKay, C. P., Pollack, J. B., & Courtin, R. 1989, *Icarus*, 80, 23, doi: [10.1016/0019-1035\(89\)90160-7](https://doi.org/10.1016/0019-1035(89)90160-7)
- McKinney, W. 2010, in *Proceedings of the 9th Python in Science Conference*, ed. S. van der Walt & J. Millman, 51–56
- Morley, C. V., Fortney, J. J., Marley, M. S., et al. 2012, *ApJ*, 756, 172, doi: [10.1088/0004-637X/756/2/172](https://doi.org/10.1088/0004-637X/756/2/172)
- Nayak, M., Lupu, R., Marley, M. S., et al. 2017, *PASP*, 129, 034401, doi: [10.1088/1538-3873/129/973/034401](https://doi.org/10.1088/1538-3873/129/973/034401)
- Niraula, P., Redfield, S., de Wit, J., et al. 2018, arXiv e-prints. <https://arxiv.org/abs/1812.09227>
- Oklopčić, A., Hirata, C. M., & Heng, K. 2016, *ApJ*, 832, 30, doi: [10.3847/0004-637X/832/1/30](https://doi.org/10.3847/0004-637X/832/1/30)
- . 2017, *ApJ*, 846, 91, doi: [10.3847/1538-4357/aa8630](https://doi.org/10.3847/1538-4357/aa8630)
- Pérez, F., & Granger, B. E. 2007, *Computing in Science & Engineering*, 9
- Pollack, J. B., Rages, K., Baines, K. H., et al. 1986, *Icarus*, 65, 442, doi: [10.1016/0019-1035\(86\)90147-8](https://doi.org/10.1016/0019-1035(86)90147-8)
- Price, M. J. 1977, *Reviews of Geophysics and Space Physics*, 15, 227, doi: [10.1029/RG015i002p00227](https://doi.org/10.1029/RG015i002p00227)
- Saitoh, N., Imasu, R., Ota, Y., & Niwa, Y. 2009, *Journal of Geophysical Research (Atmospheres)*, 114, D17305, doi: [10.1029/2008JD011500](https://doi.org/10.1029/2008JD011500)
- Snook, K. J. 1999, PhD thesis, STANFORD UNIVERSITY
- Sorensen, C. M., Heinson, Y. W., Heinson, W. R., Maughan, J. B., & Chakrabarti, A. 2017, *Atmosphere*, 8, 68
- Spergel, D., Gehrels, N., Breckinridge, J., et al. 2013, arXiv e-prints. <https://arxiv.org/abs/1305.5422>
- sqlite3 Development Team. 2019, DB-API 2.0 interface for SQLite databases
- Sromovsky, L. A. 2005, *Icarus*, 173, 254, doi: [10.1016/j.icarus.2004.08.008](https://doi.org/10.1016/j.icarus.2004.08.008)
- Sromovsky, L. A., Fry, P. M., Hammel, H. B., et al. 2009, *Icarus*, 203, 265, doi: [10.1016/j.icarus.2009.04.015](https://doi.org/10.1016/j.icarus.2009.04.015)
- Stamnes, K., Tsay, S.-C., Jayaweera, K., & Wiscombe, W. 1988, *ApOpt*, 27, 2502, doi: [10.1364/AO.27.002502](https://doi.org/10.1364/AO.27.002502)
- STScI Development Team. 2013, pynphot: Synthetic photometry software package, Astrophysics Source Code Library. <http://ascl.net/1303.023>
- Sudarsky, D., Burrows, A., Hubeny, I., & Li, A. 2005, *ApJ*, 627, 520, doi: [10.1086/430206](https://doi.org/10.1086/430206)
- Thelen, A. E., Nixon, C. A., Chanover, N. J., et al. 2019, *Icarus*, 319, 417, doi: [10.1016/j.icarus.2018.09.023](https://doi.org/10.1016/j.icarus.2018.09.023)
- Thomas, G. E., & Stamnes, K. 2002, *Radiative Transfer in the Atmosphere and Ocean*, 546
- Toon, O. B., McKay, C. P., Ackerman, T. P., & Santhanam, K. 1989, *J. Geophys. Res.*, 94, 16287, doi: [10.1029/JD094iD13p16287](https://doi.org/10.1029/JD094iD13p16287)
- Toon, O. B., Pollack, J. B., & Sagan, C. 1977, *Icarus*, 30, 663, doi: [10.1016/0019-1035\(77\)90088-4](https://doi.org/10.1016/0019-1035(77)90088-4)
- Valdes, F., Gupta, R., Rose, J. A., Singh, H. P., & Bell, D. J. 2004, *ApJS*, 152, 251, doi: [10.1086/386343](https://doi.org/10.1086/386343)
- Villanueva, G. L., Smith, M. D., Protopapa, S., Faggi, S., & Mandell, A. M. 2018, *JQSRT*, 217, 86, doi: [10.1016/j.jqsrt.2018.05.023](https://doi.org/10.1016/j.jqsrt.2018.05.023)

- Waldmann, I. P., Tinetti, G., Rocchetto, M., et al. 2015, ApJ, 802, 107, doi: [10.1088/0004-637X/802/2/107](https://doi.org/10.1088/0004-637X/802/2/107)
- Walt, S. v. d., Colbert, S. C., & Varoquaux, G. 2011, Computing in Science & Engineering, 13, 22
- Webber, M. W., Lewis, N. K., Marley, M., et al. 2015, ApJ, 804, 94, doi: [10.1088/0004-637X/804/2/94](https://doi.org/10.1088/0004-637X/804/2/94)
- Wiscombe, W. J. 1977, Journal of Atmospheric Sciences, 34, 1408, doi: [10.1175/1520-0469\(1977\)034\(1408:TDMRYA\)2.0.CO;2](https://doi.org/10.1175/1520-0469(1977)034(1408:TDMRYA)2.0.CO;2)
- Yelle, R. V., Doose, L. R., Tomasko, M. G., & Strobel, D. F. 1987, Geophys. Res. Lett., 14, 483, doi: [10.1029/GL014i005p00483](https://doi.org/10.1029/GL014i005p00483)
- Zhang, F., Liu, K., Yang, Q., Wu, K., & Zhao, J.-Q. 2017, Advances in Meteorology, 2017
- Zhang, M., Chachan, Y., Kempton, E. M.-R., & Knutson, H. A. 2019, PASP, 131, 034501, doi: [10.1088/1538-3873/aaf5ad](https://doi.org/10.1088/1538-3873/aaf5ad)

APPENDIX

A. LIST OF ALL MODELING RECOMMENDATIONS

In §3 we explored PICASO’s sensitivities to single scattering phase function, multiple scattering phase function, and Raman scattering methodology. Throughout the text, we outlined our modeling suggestions. Here, we aggregate those recommendations into a single table. In this version of PICASO, these represent the current radiative transfer defaults.

- **Single Scattering:**

- Use default specification for direct scattering (`TTHG_Ray`)
- Fit for the functional form of the fraction, f , of forward to back scattering according to the problem being addressed.
- See Table 1 for a list of pros/cons

- **Multiple Scattering:**

- For planet cases with some degree of asymmetric cloud scatterers, always use N=2 Legendre polynomial expansion with the δ -Eddington correction.

- **Raman Scattering:**

- Choose Pollack et al. methodology with Oklopčić et al. (2016) cross sections.
- Choose a stellar spectrum that matches the level of resolution needed
- The user will experience slight compute speed losses for a single run depending largely on the stellar/planet resolution chosen. However, because these shifts only need to be computed once, adding this Raman scattering methodology is not a computational burden.

- **Phase Geometry:**

- The default number of integration angles is 10 Gauss and 10 Chebyshev angles. If the user is particularly interested in exploring scattering effects at high cosine angle (e.g. near planet limb), it would be beneficial to increase the number of planet facets despite the decrease in computation speed.

B. OPACITY DATABASE

For this version of the code, PICASO contains a database of opacities that are hosted on `GitHub`. As summarized in Freedman et al. (2008), our molecular opacities are computed on a 1060 point pressure-temperature grid from 0.3-1 μ m. Currently this database contains molecular opacity from: CH₄, CO₂, CrH, FeH, H₂O, H₂S, K, Li, NH₃, Na, Rb, TiO, and VO. Notably, for CH₄ we include the visible methane following Karkoschka (1994). For continuum absorption, we include H bound-free, H free-free, H₂⁻, H₂-CH₄, H₂-H, H₂-H₂, H₂-He, H₂-N₂. We also include Rayleigh scattering from H₂, He, and CH₄, and Raman scattering from H₂ (Oklopčić et al. 2016).

Our opacity database is constructed in `sqlite3` format. `sqlite3` is a user-friendly, python-based module for the C-library, `SQLite`. After testing several database formats (`json`, `hdf5`, `ascii`, `sqlalchemy`), `SQLite` was chosen because it is a lightweight disk-based database that does not require a separate server process. Additionally, as we expand our opacity database it will be trivial to port over this smaller `SQLite` database to another format that can handle much larger data structures. We provide a full tutorial on how to query and construct `sqlite3` databases⁵. If users follow our recipe, they can swap in any molecular opacities without needing any code modifications.

⁵ </>:Opacity Tutorial